3D Printed Scaffolds for Monolithic Aerogel Photocatalysts with Complex Geometries

Schreck, Murielle; Kleger, Nicole; Matter, Fabian; Kwon, Junggou; Tervoort, Elena; Masania, Kunal; Studart, André R.; Niederberger, Markus

DOI
10.1002/smll.202104089

Publication date
2021

Document Version
Final published version

Published in
Small

Citation (APA)
Schreck, M., Kleger, N., Matter, F., Kwon, J., Tervoort, E., Masania, K., Studart, A. R., & Niederberger, M. (2021). 3D Printed Scaffolds for Monolithic Aerogel Photocatalysts with Complex Geometries. *Small*, *17*(50), Article 2104089. https://doi.org/10.1002/smll.202104089

NANO · MICRO small
www.small-journal.com

3D Printed Scaffolds for Monolithic Aerogel Photocatalysts with Complex Geometries

*Murielle Schreck, Nicole Kleger, Fabian Matter, Junggou Kwon, Elena Tervoort, Kunal Masania, André R. Studart, and Markus Niederberger**

Monolithic aerogels composed of crystalline nanoparticles enable photocatalysis in three dimensions, but they suffer from low mechanical stability and it is difficult to produce them with complex geometries. Here, an approach to control the geometry of the photocatalysts to optimize their photocatalytic performance by introducing carefully designed 3D printed polymeric scaffolds into the aerogel monoliths is reported. This allows to systematically study and improve fundamental parameters in gas phase photocatalysis, such as the gas flow through and the ultraviolet light penetration into the aerogel and to customize its geometric shape to a continuous gas flow reactor. Using photocatalytic methanol reforming as a model reaction, it is shown that the optimization of these parameters leads to an increase of the hydrogen production rate by a factor of three from 400 to 1200 µmol g^{-1} h^{-1}. The rigid scaffolds also enhance the mechanical stability of the aerogels, lowering the number of rejects during synthesis and facilitating handling during operation. The combination of nanoparticle-based aerogels with 3D printed polymeric scaffolds opens up new opportunities to tailor the geometry of the photocatalysts for the photocatalytic reaction and for the reactor to maximize overall performance without necessarily changing the material composition.

1. Introduction

To secure the survival of our heavily polluted planet, we need to build a sustainable energy system.[1] Using hydrogen as a clean and renewable energy carrier, produced from sustainable and abundant energy sources, is a promising solution.[2] The combustion of hydrogen does not release any greenhouse gases into our atmosphere.[3] With focus on the photocatalytic production of hydrogen, the challenge is to find the right materials, synthesize them with the appropriate morphology and process them into a form that enables efficient photocatalysis. From a materials point of view, most of the research is dedicated to heterogeneous photocatalysis using semiconducting photocatalysts.[4] Kudo and Miseki compiled a large collection of different photocatalyst materials ranging from various metal oxides to metal (oxy)sulfides and metal (oxy)nitrides.[5] In spite of this immense compositional diversity, the largely available, cheap, stable, and nontoxic titanium dioxide (TiO_2) is still one of the most studied photocatalysts, regardless of its activity being limited to ultraviolet (UV) light illumination and its unfavorable fast electron hole recombination.[6]

In addition to the materials selection, the morphology of the photocatalyst also plays an important role, because a large surface area, which exposes many adsorption sites to the environment, is crucial.[3] Nanostructures with particle-,[7–9] rod-,[10–12] tube-,[13–15] or sheet-like[16–18] morphology provide a large surface-to-volume ratio and thus have been found to be ideal structures for photocatalysis. However, most nanoparticles are used in powder form, which has the disadvantage that such photocatalytic nanostructures tend to agglomerate and that extraction of the photocatalyst from the reaction medium for recycling is challenging.[19] Consequently, processing of the nanoparticles into thin films[20,21] or their immobilization on 3D, photocatalytically nonactive templates such as foams,[22] sponges,[23] mesoporous silica,[24,25] electrospun nanofibers[26–28] or hydroxyapatite[29] has been pursued.[3] However, a significant reduction in surface area and number of adsorption sites, both of which are detrimental to photocatalytic activity, is inevitable.[19] A solution to this problem is the fabrication of template-free, macroscopic, 3D structures entirely made of the photocatalytic material. Examples along these lines include 3D porous g-C_3N_4,[30] mesoporous TiO_2 foams,[31] graphene oxide (GO) sponges,[32] porous g-C_3N_4 monoliths,[33] MoS_2/rGO aerogels,[34] CN aerogels,[35] or Au–Pt–TiO_2 aerogels.[36] Unfortunately, the

M. Schreck, F. Matter, J. Kwon, E. Tervoort, M. Niederberger
Laboratory for Multifunctional Materials
Department of Materials
ETH Zürich
Vladimir-Prelog-Weg 5, Zürich 8093, Switzerland
E-mail: markus.niederberger@mat.ethz.ch
N. Kleger, K. Masania,[+] A. R. Studart
Complex Materials
Department of Materials
ETH Zürich
Vladimir-Prelog-Weg 5, Zürich 8093, Switzerland

The ORCID identification number(s) for the author(s) of this article can be found under https://doi.org/10.1002/smll.202104089.

[+]Present address: Shaping Matter Lab, Faculty of Aerospace Engineering, TU Delft, Kluyverweg 1, Delft 2629 HS, Netherlands

DOI: 10.1002/smll.202104089

advantages of the 3D architecture are often not fully exploited, because the photocatalysts are usually dispersed in the liquid reaction medium for the photocatalytic measurements, resulting in pulverization of the samples. In addition to destroying the 3D structure, the use of a solvent has some other significant disadvantages. The intensity of the illumination decreases quickly due to light absorption by the liquid or reflection by bubbles in the liquid. This reduction in light intensity leads to a decrease in the photocatalytic efficiency of the process. Additionally, photocorrosion and, consequently, deactivation of the photocatalyst is enhanced in liquid phase.[3,37,38] Fortunately, these drawbacks can be avoided by working in the gas phase.

Among the 3D structures that solely consist of photocatalytic materials, nanoparticle-based aerogels[39–41] have a huge potential as photocatalysts for gas phase reactions. The size-specific properties of the nanoparticle building blocks are fully maintained in the macroscopic network. Nanoparticle-based aerogels thus make it possible to combine the intrinsic advantage of material properties (good photocatalytic performance) with the benefits of the morphology (large surface area – many active sites for the interaction of photocatalyst with reactant, large open porosity – high, continuous mass transport, and optimized gas flow), resulting in an efficient monolithic and shapeable photocatalyst.[38,42] For the first step in the synthesis of a nanoparticle-based aerogel, we need a stable, highly concentrated dispersion of nanoparticles. The dispersion is destabilized using a trigger to form a gel, which is subsequently supercritically dried to maintain the pore structure. The path from colloidal dispersions to aerogels has been comprehensively outlined recently.[43] However, even under optimized gelling conditions and considering that the photocatalytic tests are performed in the gas phase, the mechanical stability of the aerogel monoliths remains an issue for handling and operation, because more than 97% of the monoliths is air and the rest is comprised of very thin chains of individual nanoparticles just 3–4 nm in diameter.[43] Furthermore, the monoliths must not contain large cracks that could cause them to fall apart completely and prevent the gas from interacting efficiently with the aerogel. These high quality standards make greatest demands to the synthesis and lower the yield. One possibility to increase the mechanical stability of aerogels is to apply a sintering step. However, sintering affects the microstructure and can lead to a reduction or complete loss of translucency, which is detrimental for the photocatalytic application of the aerogels. In addition, shrinkage reduces the surface area and the number of adsorption and active sites, which also lowers the photocatalytic efficiency.[42–44]

To address these issues and to introduce more flexibility in the design of 3D photocatalysts, we present here the use of 3D printed polymeric structures as scaffolds for nanoparticle-based aerogels. Although the aerogels are self-supporting and the scaffolds do not act as templates, the combination of a rigid structure with a fragile aerogel leads to an enhancement of the mechanical stability, which not only increases the yield of the aerogel synthesis, but also greatly facilitates the handling of the monoliths during photocatalytic tests. We demonstrate this using TiO_2 nanoparticles loaded with palladium (Pd) nanoparticles. The Pd nanoparticles act as electron sink and keep the charge carriers separated until they participate in the photocatalytic redox reactions. The 3D printed scaffolds and their systematically tunable geometries provide unique opportunities to define the gas flow through the monoliths, to study the penetration depth of the UV light into the aerogels, and to optimally adapt the geometry of the monoliths to a specific reactor design. All these parameters are fundamental for the understanding and systematic improvement of the photocatalytic process. The benefit of our strategy is confirmed by the successful application of the scaffold-supported TiO_2–Pd aerogels as photocatalysts for methanol (MeOH) reforming to produce hydrogen gas at high rates.

2. Results and Discussion

2.1. 3D Printed Polymeric Structures as Scaffolds for Nanoparticle-Based Aerogels

A major advantage of the 3D printed polymeric scaffolds is that they improve the mechanical stability of the nanoparticle-based aerogels during the synthesis as well as during the investigation of their photocatalytic activity. In fact, the handling of the aerogel monoliths is greatly facilitated by the scaffolds. Another important benefit of the scaffolds is that they affect the hierarchical architecture of the aerogels and control the gas flow, which can have an immense impact on the photocatalytic performance. Systematic variation of the geometrical design of the macroscopic aerogel monoliths with respect to light absorption and photocatalyst mass allows us to determine the optimal fit for our customized continuous gas flow reactor (**Scheme 1**) and, hence, to maximize the hydrogen production rate for this specific setup.

To explore the potential of this approach, we systematically study different scaffold geometries (**Figure 1**), which can easily be 3D printed. The scaffolds were manufactured from a commercially available acrylate-based resin using a desktop digital light processing printer. A geometrical structure based on the diamond lattice acts as the standard (or reference) scaffold (Figure 1a,e). To better understand the gas flow and the reactant transport through the network of the photocatalyst inside the reactor, we use a punched tube scaffold (Figure 1d). Compared to the standard scaffold, it contains a tube along the middle axis, which is closed at the end, but contains holes that guide the gas into the aerogel. In this way, we can enforce an enhanced interaction of the gas with the framework of the photocatalyst. Finally, scaffolds with dense polymeric cores of different diameters (Figure 1b,c,f) are used to examine the effect of UV light penetration into the aerogel monoliths. By varying the diameter of the cores, we can optimally match the thickness of the aerogel layer to the depth of light penetration, which helps to minimize the amount of nonilluminated and, hence, inactive photocatalyst.

2.2. Characterization of the Aerogels

The selection of TiO_2 and Pd nanoparticles as building blocks for the aerogels is based on their well-known photocatalytic activity for hydrogen production via MeOH reforming.[42,45–47] The presynthesized, Trizma-functionalized TiO_2 nanoparticles and the Pd nanoparticles are cogelled around the polymeric scaffold, which is placed inside a quartz tube (Figure 1g). It

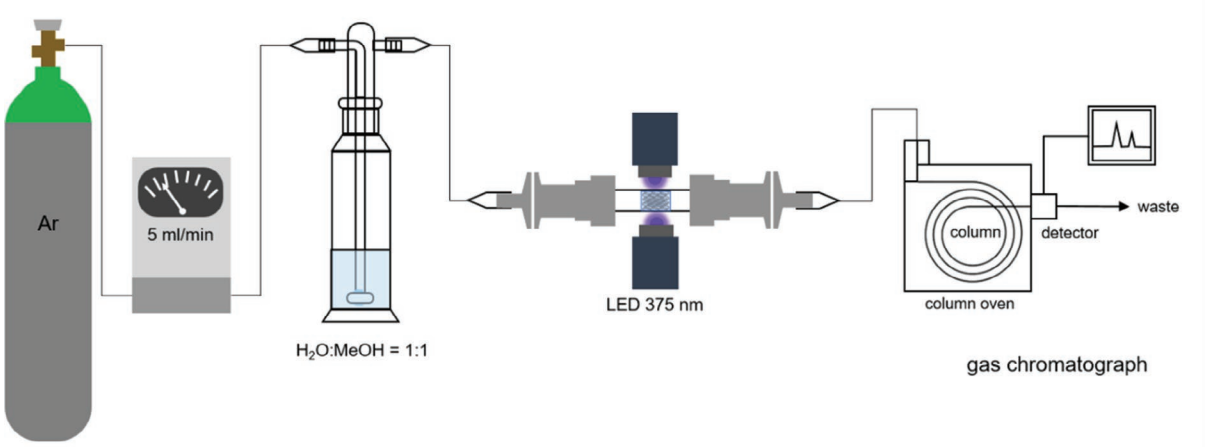

Scheme 1. Customized continuous gas flow reactor setup: Ar gas, controlled by a mass flow meter (5 mL min^{-1}), is enriched with water and MeOH (water:MeOH = 1:1 v/v). The humidified gas flows through the aerogel sample inside a quartz tube, which is illuminated by two LEDs (375 nm). The outlet stream is analyzed by a gas chromatograph.

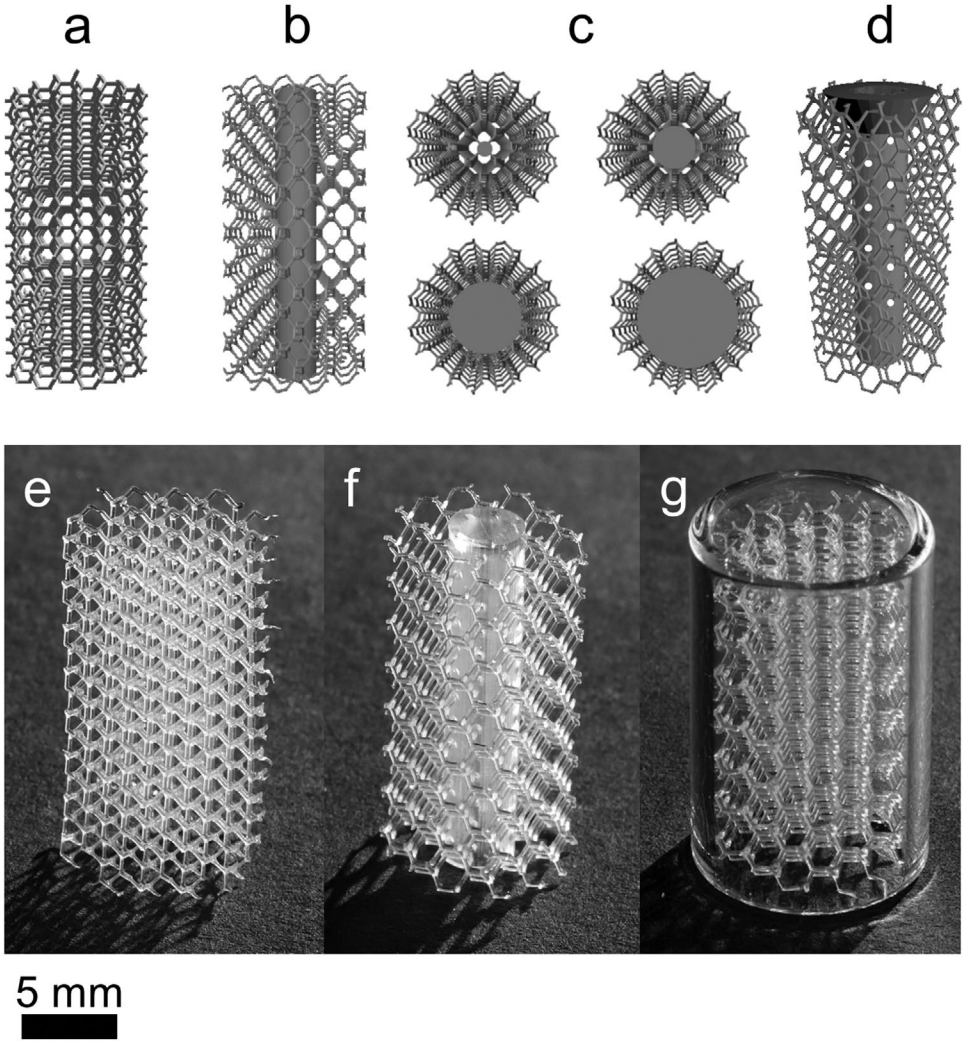

Figure 1. CAD drawings of different scaffold geometries: a) standard scaffold, b) scaffold with core of c) various diameters (1, 3, 5, 7 mm), and d) punched tube scaffold. Digital photographs of e) a standard scaffold, f) a scaffold with a 3 mm core and of g) a standard scaffold in a quartz tube. The scale bar applies to images (e)–(g).

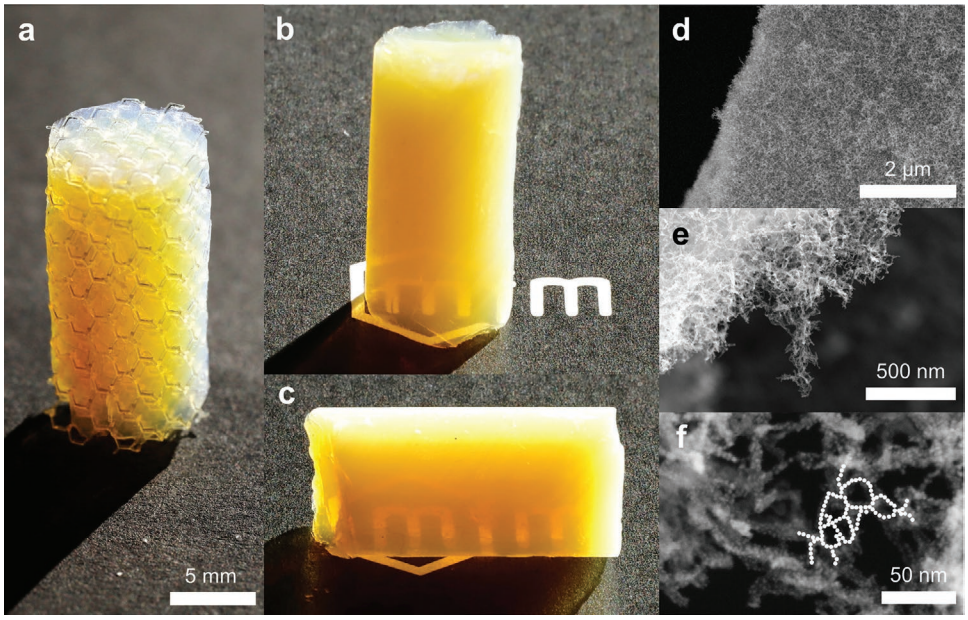

Figure 2. Photographs of translucent cm-sized aerogel monoliths a) with and b,c) without an embedded standard scaffold and d–f) SEM images of the TiO_2–Pd aerogel morphology at different magnifications. The pearl-necklace-like structure of the nanoparticle network is highlighted with white filled circles in (f).

is important to clarify that the scaffold is only a mechanical reinforcement and a means to influence the geometry of the aerogel (**Figure 2**a). The scaffold does not act as a template for the nanoparticles that form the 3D network by pure self-assembly. Photographs in Figure 2b,c are proof that this network of nanoparticles is strong enough to produce self-supporting, translucent, cm-sized aerogel monoliths. Therefore, morphological and compositional characterization was done on aerogels without a scaffold. The scanning electron microscopy (SEM) images in Figure 2d–f show the finely branched network composed of pearl-necklace-like chains of individual nanoparticles. Nitrogen gas sorption analysis presents a surface area of 549 $m^2\ g^{-1}$ and a pore size distribution with a maximum at around 34 nm (Figure S1, Supporting Information). When measuring powder X-ray diffraction (XRD) of the TiO_2–Pd aerogel, only anatase TiO_2 is observed (Figure S2, Supporting Information), because the concentration of the cocatalyst is too small to be detected by XRD measurements. The crystallite size of the TiO_2 nanoparticles is on average 3 nm, calculated from the full width at half maximum of the (101) reflection using the Scherrer equation. With X-ray photoelectron spectroscopy we prove that Pd is present in the TiO_2–Pd aerogel (Figure S3, Supporting Information). The measured Pd concentration of 0.04 at% corresponds to 0.18 wt%, which agrees well with the initially added amount of 0.17 wt%. Whereas the particle size of the TiO_2 nanoparticles coincides with the crystallite size, which means that each particle is a single crystallite, particle size and crystallite size of Pd nanoparticles differ. The XRD measurements of Pd nanoparticles alone reveal a crystallite size of on average 7.7 nm, calculated from the full width at half maximum of the (111) reflection at 2 Theta = 40° (Figure S4, Supporting Information). According to SEM, the diameter of the Pd nanoparticles is between 50 and 200 nm (Figure S5, Supporting Information). Therefore, each Pd nanoparticle is an agglomerate composed of smaller crystallites.

2.3. Removal of Surface-Adsorbed Organics

One problem of nanoparticle-based aerogels is that organic residues remain attached to the surface of the nanoparticles even after supercritical drying, which is the result of the wet-chemical synthesis route performed in an organic medium. These organic species interfere with the photocatalytic hydrogen production process.[43] Their decomposition under UV light irradiation during photocatalysis contributes to the hydrogen production, falsifying the results. At the same time, the decomposition products lower the activity of the photocatalyst by blocking active sites. One solution to this issue is to subject the aerogels to a UV pretreatment in air to remove the organic residues. We investigate the effect of such a UV pretreatment on the photocatalytic activity using a TiO_2–Pd aerogel that is not supported by a scaffold. **Figure 3** displays the hydrogen production from MeOH and water in ppm with a logarithmic scale over time under a pure Ar gas flow (no MeOH and water) and under Ar gas flow enriched with MeOH and water. The photocatalytic hydrogen evolution is shown for an as-synthesized (black) and a UV pretreated TiO_2–Pd (red) aerogel. During the first illumination phase (Ar only), the as-synthesized sample produces a lot of hydrogen, which obviously originates from the decomposition of surface organics. The hydrogen production decreases over time, because the source of hydrogen atoms decreases with increasing decomposition of the organics. During the second illumination phase (Ar + MeOH + water), the produced amount of hydrogen stays constant over time. This is an indication that the hydrogen gas stems from the photocatalytic reaction of MeOH and water. In comparison,

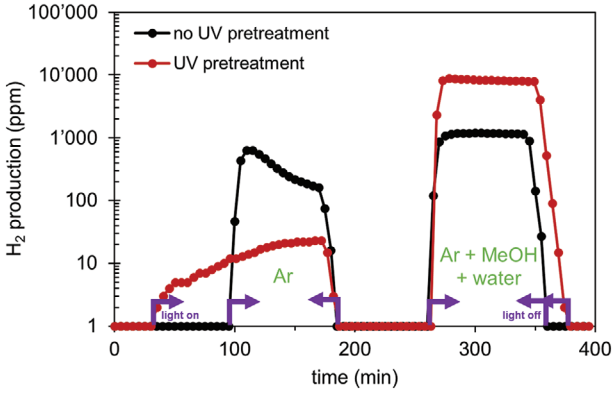

Figure 3. Amount of absolute hydrogen production in ppm produced over time by an as-synthesized (black) and a UV pretreated (red) TiO_2–Pd aerogel. Hydrogen production is depicted in a logarithmic scale. The illumination time is indicated with violet arrows. During the first illumination phase, only Ar gas flows through the aerogel. During the second illumination phase, the Ar gas is humidified with MeOH and water.

the UV pretreated sample produces much less hydrogen during the first illumination phase. We assume that this hydrogen originates from surface-adsorbed species that are left even after the UV pretreatment under ambient conditions. During the second illumination phase, when the photocatalytic hydrogen production process from MeOH and water takes place, the amount of produced hydrogen is almost an order of magnitude larger for the UV pretreated sample compared to the as-synthesized sample. This is because the oxidation of organics of the as-synthesized sample under UV light irradiation during the first illumination phase (Ar only) presumably blocks the active sites of the photocatalyst and thus reduces its photocatalytic activity. Consequently, pretreatment of the nanoparticle-based aerogels with UV light in air to remove surface-adsorbed organics is crucial for their applications in photocatalysis. We find that a treatment of 20 h is ideal to minimize the organic residues, which is confirmed by thermogravimetric analysis (TGA) measurements (Figure S6, Supporting Information).

2.4. Influence of Scaffolds on Mechanical Stability and Photocatalytic Performance

The 3D printed polymeric scaffolds minimize disintegration of the gels and aerogels when handling them during their fabrication process and afterward during photocatalytic tests. The mechanical stability is defined here by the yield of aerogels that survive a 24 h photocatalytic analysis under constant gas flow and constant illumination with UV light. The yield of intact monoliths increases from roughly 40% to almost 100% when scaffolds are introduced during the fabrication process, showing how beneficial the scaffolds are in terms of reducing the number of rejects, thus saving valuable material, cost, and time.

While the scaffolds fulfill an important task in the mechanical stabilization of the aerogels, the question arises whether or not they also have an effect on the photocatalytic activity. In this context it is important to note that the scaffold is photocatalytically inert, i.e., illumination of the scaffold in the presence of Ar, MeOH, and water did not result in the formation of any detectable products from the decomposition of the scaffold or any additional species from side reactions.

For the following discussion of the different scaffold geometries and their influence on the photocatalytic activity, it is important to clarify some points in advance. After placing the cylindrical aerogel monolith in the quartz tube of the reactor, they are fixed with Teflon and NBR O-rings (see the Experimental Section and the discussion by Rechberger and Niederberger[38]), which hold the aerogel in place, but also help to guide the gas into the aerogel. The aerogels are slightly smaller than the inner diameter of the quartz tube and this creates a small gap between the two components, which is not sealed further. We therefore assume that part of the gas does not enter the aerogel from the front, but flows along the gap (**Scheme 2**a) and then, at least partially, diffuses laterally into the aerogel. It can be expected that this bypass effect is similar for all aerogels investigated in this study, since they are all produced in the same mold, undergo the same shrinkage during supercritical drying, and consequently the gap between the monolith and the quartz tube is rather similar for all samples. We are therefore convinced that the different hydrogen production rates, as we will discuss in the following sections, are indeed due to the variations in scaffold geometries.

First, we examine the influence of the standard scaffold structure on the photocatalytic performance of the aerogel. We observe that the photocatalytic efficiency of aerogels with scaffolds is higher than of those without a supporting structure. This finding is shown in **Figure 4**, displaying the hydrogen production in ppm normalized to the amount of photocatalyst in mg. This plot also gives an indication about the long-term stability of the photocatalytic process. After a strong decrease of the hydrogen production within the first 1–2 h, the activity of the photocatalyst only decreases around 5% to 10% over the course of the next 14 h. The reason for this initial hydrogen peak is not clear yet and subject to further studies. However, this peak is not an artefact and Figure 4 is representative for all measured data.

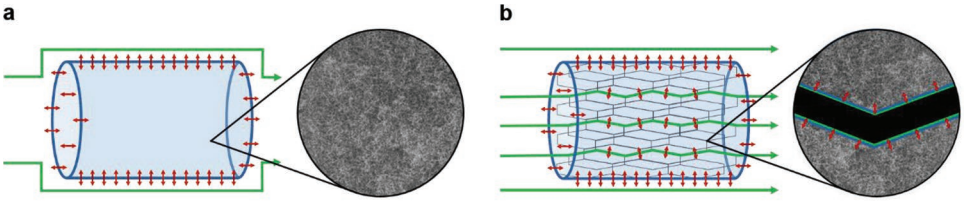

Scheme 2. Proposed gas flow and reactant transport in and around aerogel monoliths a) without and b) with a scaffold embedded in the aerogel. The gas flow is indicated by green arrows and the gas diffusion by red arrows.

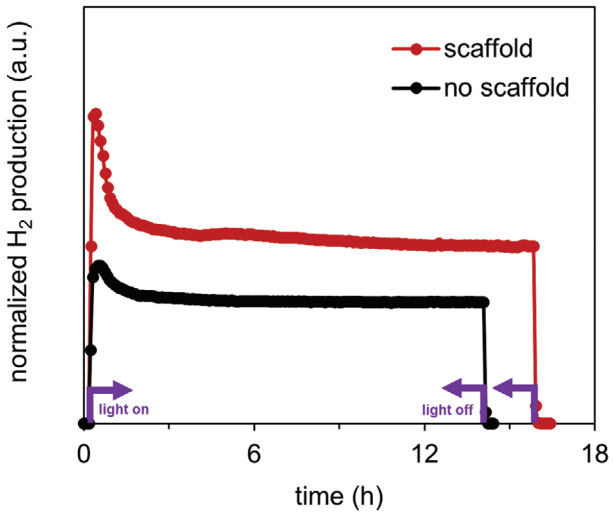

Figure 4. Comparison of hydrogen production between an aerogel with (red) and without (black) mechanical reinforcement by a 3D printed polymeric scaffold. The hydrogen production is normalized to the mass of the aerogel photocatalyst and measured over time of illumination, which is indicated by the violet arrows.

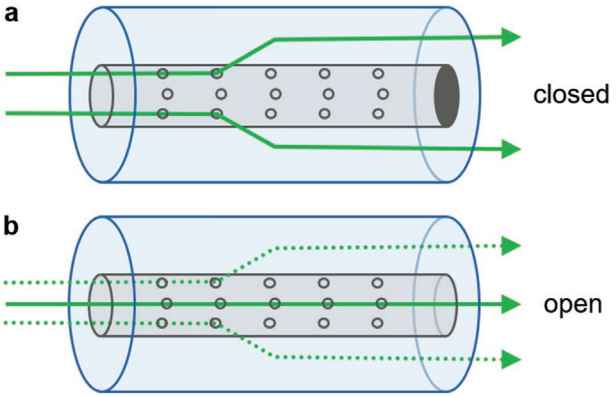

Scheme 3. Possible paths of the gas molecules (solid and dotted green arrows) through a) the punched tube scaffold (pTS) with a closed end and b) the punched tube scaffold with an open end. For the sake of an easier illustration, the struts of the scaffolds are not displayed in this scheme.

The explanation for the difference in photocatalytic performance of an aerogel with and without scaffold is related to the question of how much MeOH and water, which are transported by the Ar gas, can interact with the photocatalytic material. We propose that introducing a scaffold into the aerogel leads to the formation of cracks in the aerogel along the scaffold struts during the UV pretreatment removing the organic residues. It is somewhat counterintuitive that cracks improve the photocatalytic performance. However, it was reported before that the small pore size in aerogels prevents an efficient gas flow through the monolith, limiting the interaction of the gas molecules to the outer surface of the aerogel.[48] In our case, however, the continuous cracks along the boundary between aerogel and scaffold facilitate a hierarchical flow behavior at two length scales. The primary flow can transport reactants along the aerogel scaffold interface and a secondary flow transports reactants into the pore structure of the aerogel. If we define the surface of the monolith body as the primary surface (dark blue lines in Scheme 2) and the surface originating from the nanoparticle network as the secondary surface (bright blue area in Scheme 2), then the mass transport of the gas molecules from outside the aerogel (primary surface) into its pore structure (secondary surface) occurs mainly via a diffusion mechanism (red arrows in Scheme 2). For the aerogels with scaffolds, the cracks along the scaffold struts separating scaffold and aerogel increase the amount of primary surface of the photocatalyst and guide the gas into the inner part of the aerogel, bringing it into contact with its secondary surface. A larger primary surface leads to more diffusion pathways, improving the interaction of the reactant molecules with the photocatalyst and, therefore, to a better photocatalytic performance. The presence of such cracks, which enhance the diffusion of reactants into the aerogel, is difficult to prove by experimental techniques such as electron microscopy. Any specimen preparation carries the risk of introducing additional cracks into the delicate aerogel structure, which would be indistinguishable from the initial cracks along the scaffold struts. However, what we can do to indirectly demonstrate the importance of cracks and the resulting enhanced diffusion is to study the influence of a macroscopically large channel that guides the gas into the aerogel monolith. Of course, this is an extremely simplified model, but if such a large channel already affects the hydrogen production rate, then it is reasonable to assume that a large number of microchannels, i.e., cracks, should have a significantly larger impact.

To confirm this hypothesis, we changed the geometry of the standard scaffold to punched tube scaffolds. Using these punched tube scaffolds, we can now introduce the before mentioned macroscopically large channel into the aerogel and guide the gas into the monolith. We use two different types of punched tubes. As shown in **Scheme 3**, the tube inside the aerogel is either closed (a) or open (b) on one end and holes are punched into its sidewalls. We make sure that the gas flows first into this tube. In Scheme 3a, the gas has to exit the tube via the holes in the sidewall, because the end of the tube is closed. In this way, the gas is forced to flow through the aerogel network. In Scheme 3b, the gas is expected to flow straight through the tube and exit at the opposite open end without much interaction with the aerogel photocatalyst (solid green arrow). The data from the photocatalytic tests in **Figure 5** reveal that hydrogen is produced in both cases, which implies that the gas molecules diffuse into the aerogel network and interact with the photocatalyst whether it is forced to do so or not (dotted green arrow). Closing the tube on one end, however, increases the hydrogen production. This result together with the fact that our customized continuous gas flow reactor operates under ambient pressure (1 bar) confirms that diffusion is the main mechanism responsible for the transport of reactant molecules into the aerogel network and, therefore, determines the photocatalytic performance of the aerogel photocatalysts.

2.5. Optimizing the Geometry of the Photocatalyst

We previously identified several items as fundamental to consider when improving the efficiency of a photocatalytic gas

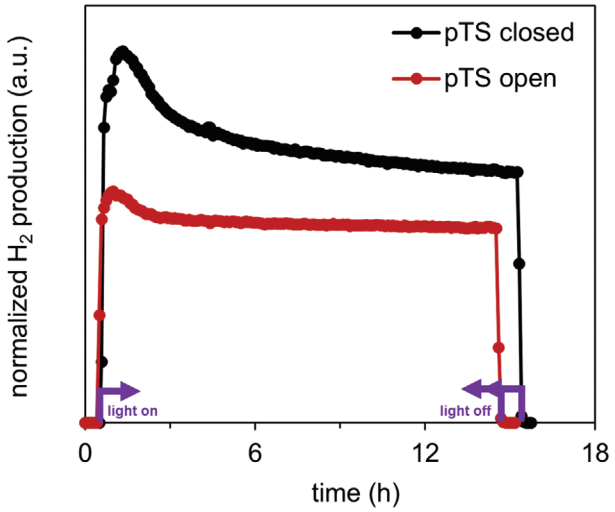

Figure 5. Comparison of hydrogen production between an aerogel synthesized around a punched tube scaffold (pTS) with closed end (black) and open end (red). The hydrogen production is normalized to the mass of the aerogel photocatalyst and measured over time of illumination, which is indicated by the violet arrows.

phase reaction.[3] These items cover gas composition and gas flow, the interaction of the gas with the photocatalyst and the photocatalytic process itself. We now propose an additional item: optimal adaptation of the geometry of the photocatalyst monolith to the reactor design, in our case a customized continuous gas flow reactor.[38] Such an adjustment can readily be achieved through 3D printed polymeric scaffolds, enabling an optimized utilization of the used illumination source. We study the influence of the path of the UV light in the radial direction of the monolith. Scaffolds with solid cores of various diameters are used to find the ideal layer thickness of the photocatalyst with respect to light absorption in the reactor. Next, we test different lengths of aerogel monoliths to optimize the illumination also in axial direction. Finally, we combine all the findings in a photocatalyst geometry that perfectly fits to our flow reactor, is illuminated in the most efficient manner and thus maximizes the hydrogen production rate.

When using macroscopically sized aerogel monoliths as photocatalysts, a fundamental question is how far the UV light can penetrate into the translucent aerogel network in radial direction. We tackle this point by illuminating the photocatalyst first from one side only, followed by illumination from two opposite sides. The amount of hydrogen production in ppm doubles in case of a two-sided illumination (Figure S7, Supporting Information). We conclude that light from just one side is not able to penetrate the full width of the monolith. To find out how far the UV light exactly penetrates into the aerogel and whether parts of it are not illuminated at all, we use scaffolds with inner solid cores of varying diameters (1, 3, 5, and 7 mm, Figure 1c), while keeping the overall diameter of 10.4 mm constant. The resulting thicknesses of the aerogel layers around the core are 4.7, 3.7, 2.7, and 1.7 mm, respectively. With this approach we are able to study the influence of the thickness of the aerogel layer, and thus of the penetration depth of the light, on the photocatalytic activity. By changing the size of the core rather than the diameter of the whole aerogel monolith, exactly the same synthesis procedure to fabricate the aerogels and the same reactor setup to measure their photocatalytic performance may be used to ensure accurate comparison. **Figure 6** shows that the aerogel layer thicknesses of 5.2 to 2.7 mm produce the same absolute amount of hydrogen in ppm while a layer thickness of 1.7 mm results in a strongly decreased hydrogen production, indicating that the UV light travels through the aerogel layer and reaches the polymeric core. This observation suggests that the UV light penetrates the aerogel more than 1.7 mm, but less than 2.7 mm.

It is important to mention that the source of the UV light is a light-emitting diode (LED), which behaves approximately like a point source and, therefore, does not illuminate the aerogels fully homogeneously. From this point source, the light falls on the surface of the aerogel and then penetrates the monolith. Due to the curvature of the sample, the distance between the

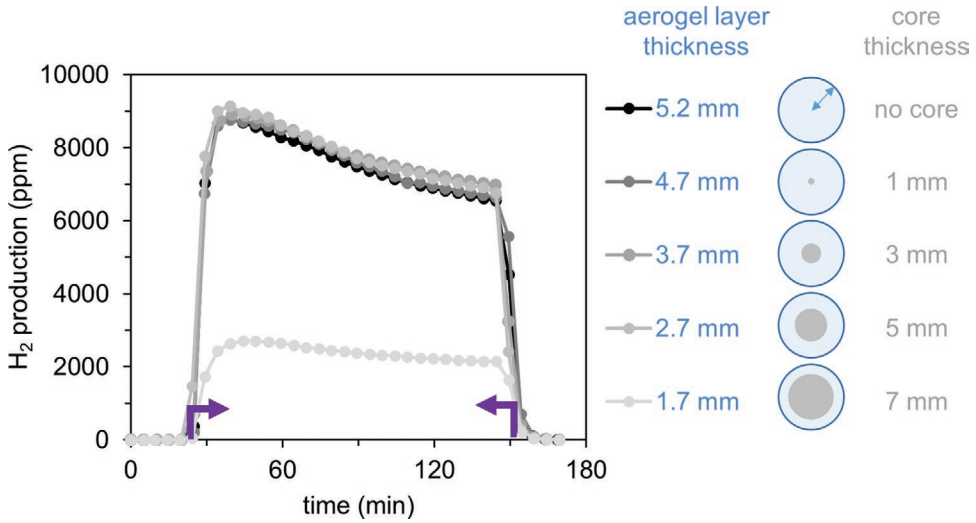

Figure 6. Comparison of the absolute hydrogen production in ppm of aerogel monoliths containing scaffolds with polymeric cores of different diameters. The violet arrows indicate the illumination time.

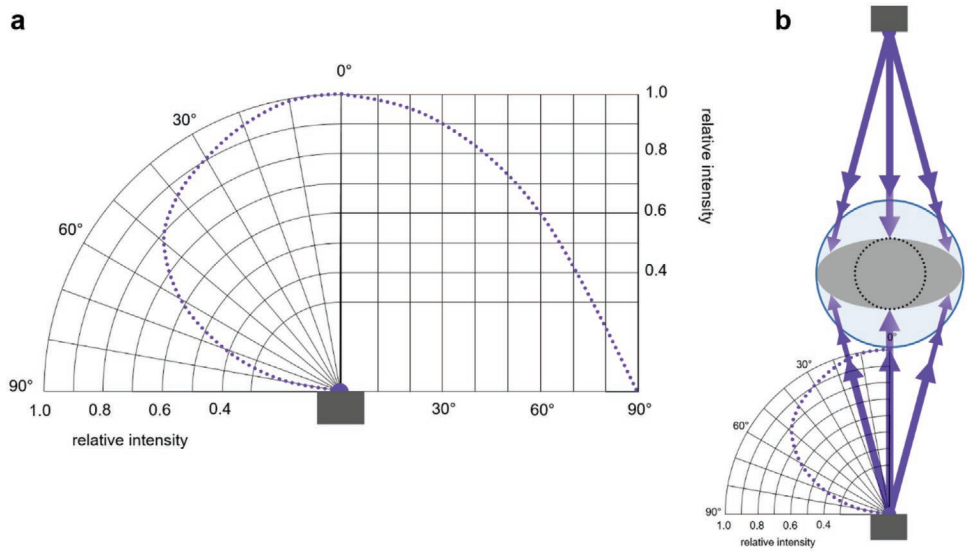

Scheme 4. a) Relative intensity of the illumination of a Thorlabs mounted high-power light-emitting diode (LED) with wavelength 375 nm versus certain angles, which deviate from the direct beam (at 0°) between the LED and the aerogel.[49] b) Illustration of the penetration of UV light into the aerogel in radial direction of the monolith. The decreasing weight of the arrow shafts indicates a decreasing intensity due to the deviation from the direct beam (a) and due to the increasing distance from the light source. The fading color of the arrows indicates an intensity loss due to interaction with the aerogel material. The black dotted line and the gray area show two different versions of geometries for the base of the scaffold core. The blue circle represents the outline of the base of the cylindrical aerogel monolith.

surface of the aerogel and the light source varies and, therefore, the intensity depends on the angle at which the light hits the sample. **Scheme 4**a displays the relative intensity of the LED at certain angles deviating from the direct beam between the LED and the aerogel.[49] Due to this angle dependence, the base of the cylindrical core of the aerogel, which is not illuminated, has the shape of an ellipse (gray in Scheme 4b) rather than that of a circle (black dotted line in Scheme 4b). The blue circle in Scheme 4b represents the outline of the base of the cylindrical aerogel monolith.

For the absolute amount of hydrogen produced, these aspects are irrelevant. However, if we consider the rate of hydrogen production, i.e., the absolute production normalized to the mass of the photocatalyst and the time of illumination, we have now the possibility to reduce the mass of inactive material without affecting the absolute hydrogen production. By eliminating the nonilluminated regions of the aerogel we can increase the rate of hydrogen production by 74% (**Figure 7**) with respect to the mass of material used.

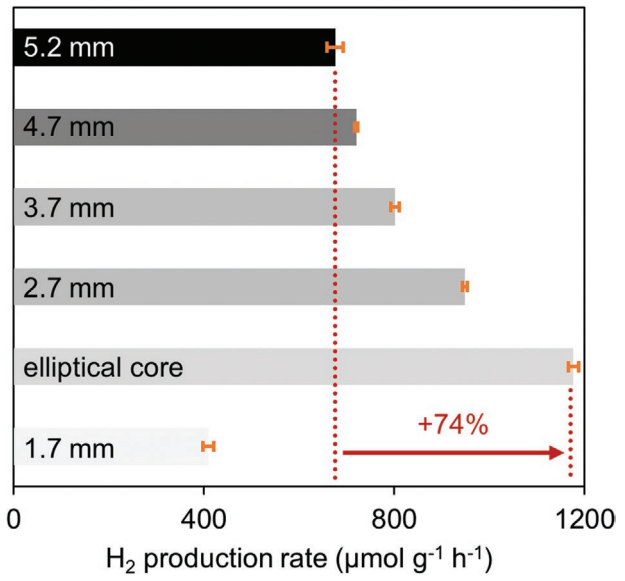

Figure 7. Average hydrogen production rate in µmol g^{-1} h^{-1} after 2 h illumination time including the mean standard deviation of TiO_2–Pd aerogels with different aerogel layer thicknesses. The increase in hydrogen production rate by 74% when decreasing the aerogel layer thickness to 2.7 mm and using an elliptical core design is indicated.

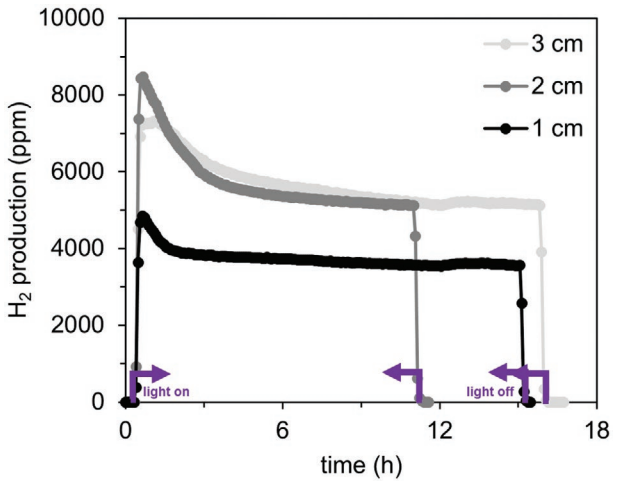

Figure 8. Comparison of absolute hydrogen production in ppm between aerogels of different lengths: 1, 2, and 3 cm. The violet arrows indicate the illumination time.

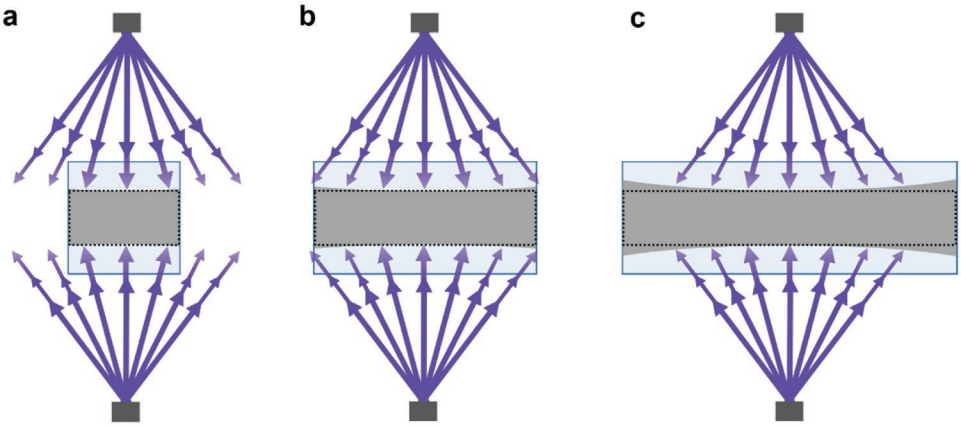

Scheme 5. a–c) Illustration of the angle of incidence on and the penetration of UV light into aerogels of different lengths (a – 1 cm, b – 2 cm, c – 3 cm), view on axial direction of the monolith. The decreasing weight of the arrow shafts indicates a decreasing intensity due to the deviation from the direct beam (see Scheme 4a) and due to the increasing distance from the light source. The fading color of the arrows indicates an intensity loss due to interaction with the aerogel network. The black dotted line shows the nonilluminated area in the case of an angle-independent illumination, the gray area shows the nonilluminated area in the case of point light sources (angle dependent). No arrows are drawn beyond a 2 cm length of the illuminated area to illustrate that this part of the illumination by the LEDs is negligible for hydrogen production. The penetration depth of the UV light does not exceed 2.7 mm, i.e., in the case of the standard scaffolds without core, the middle part of the aerogel (dotted black rectangle) remains nonactivated.

Although this result is specific for our flow reactor, we want to emphasize the general potential of how a good match between the geometry of the photocatalyst and the reactor (including an illumination system) can boost the photocatalytic performance significantly. Clearly, the flexibility of the 3D printing process makes such a design optimization readily feasible.

In addition to the illumination with a point source such as LED, we also address the length of the aerogel monolith used. The aerogel monolith should present an optimal length related to the region that can effectively be illuminated by the LEDs.

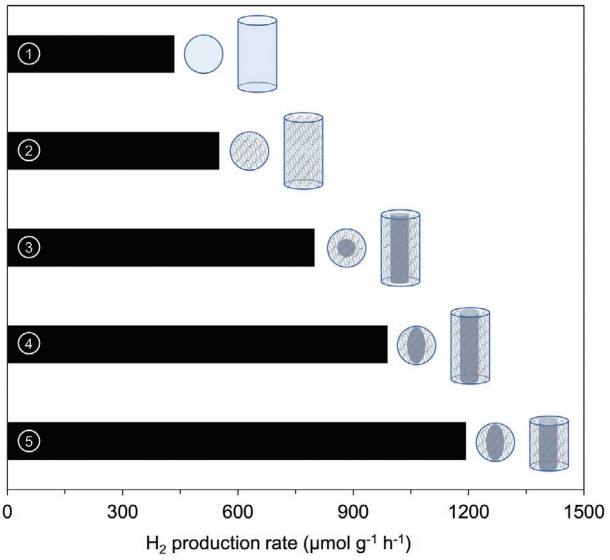

Figure 9. Hydrogen production rate in µmol g^{-1} h^{-1} after 10 h of illumination time of TiO_2–Pd aerogels synthesized around various scaffold geometries: no scaffold (1), standard scaffold (2), scaffold with solid core with circular cross-section (3), scaffold with solid core with elliptical cross-section (4), scaffold with solid core with elliptical cross-section and optimized length of 1.5 cm (5).

To study this, we synthesized 1, 2, and 3 cm long aerogels, which are supported by the corresponding standard scaffold structures. **Figure 8** displays their absolute hydrogen production over the course of up to 16 h. The 2 and the 3 cm long aerogels produce the same amount of hydrogen. We conclude that illumination beyond the length of 2 cm is not efficient enough to activate the photocatalytic material for the production of hydrogen. The reasons are visualized in **Scheme 5**. In addition to the length of the monoliths also the penetration depth of the light into the monoliths has to be considered. The volume of the nonactivated aerogel depends on the angle, at which the light arrives at the sample, i.e., a beam perpendicular to the sample has a higher penetration depth than a beam at higher angles of incidence. Hence, the volume of nonactivated material deviates slightly from a perfect cylinder, highlighted in gray in Scheme 5. We found that the deviations are negligible in all cases and therefore this effect does not contribute much to hydrogen production. Figure 8 shows that the 1 cm aerogel exhibits a smaller hydrogen production than the longer samples. If we consider the situation in Scheme 5, the UV light is obviously able to efficiently illuminate samples beyond 1 cm, but no further than 2 cm, to contribute to hydrogen production. We conclude that the optimal length of an aerogel for our continuous gas flow reactor using two point-like LEDs as UV light source is between 1 and 2 cm, and within this range the UV light intensity reaching the aerogel does not vary significantly.

Figure 9 summarizes the geometrical optimization of our aerogel monolith photocatalysts: (1 → 2) introduction of the scaffold to improve the mechanical stability, the gas flow, and reactant transport, (2 → 3) addition of a solid core with a circular cross-section to the scaffold to examine the UV light penetration in radial direction of the monolith, (3 → 4) adjusting the cross-section of the core from circular to elliptical. As a final step, we reduce the length of the scaffold with an elliptical core cross-section from 2 to 1.5 cm (4 → 5) to prove that the optimal aerogel length lies in between 1 and 2 cm. The result is shown

in Figure 9 (5), illustrating the adjustment of the length of the monolith to study the UV light penetration in axial direction of the monolith. While optimization (1 → 2) increases the absolute hydrogen production, all other adjustments to the scaffold geometry mainly allow minimizing the amount of photocatalyst, resulting in an increased hydrogen production rate, i.e., hydrogen production normalized to the mass of the photocatalyst and to the illumination time. Through these stepwise refinements, we observe that the rate increases by a factor of three from initially 400 to 1200 μmol g^{-1} h^{-1}. The 3D printed polymeric scaffolds are an invaluable means to manipulate the aerogel monoliths for photocatalytic gas phase reactions without changing the composition and morphology of the photocatalytic materials.

3. Conclusion

The 3D printing of polymeric scaffolds is a versatile tool to systematically evaluate different aerogel geometries with the same composition for optimizing the photocatalytic performance. Scaffolds are used to facilitate the hierarchical flow behavior inside the aerogel while simultaneously preventing their disintegration. We propose that by using the scaffolds we can define the path for the gas to flow through the aerogel network and, consequently, increase the opportunity for diffusion of reactant molecules inside the aerogel. This leads to a better photocatalytic performance. Further, we take advantage of the scaffolds to investigate the UV light penetration in radial and axial direction of the aerogel monoliths. This data helps to minimize the amount of unutilized material, which is not illuminated because of the reactor design and chosen light source. Thus, we are able to maximize the hydrogen production rate (hydrogen production normalized to the mass of the photocatalyst and to the illumination time) specifically for our customized continuous gas flow reactor. We emphasize the importance of the proper fit between photocatalyst geometry and reactor design, which is especially critical when working with 3D photocatalysts. With carefully tailored 3D printed polymeric scaffolds, the geometry of any 3D, template-free, self-supporting photocatalyst can be adjusted to maximize its performance in existing reactors built for photocatalysis in the gas phase.

4. Experimental Section

Materials: Titanium (IV) tetrachloride ($TiCl_4$, 99.9% trace metals basis), anhydrous benzyl alcohol (BnOH, 99.8%), benzyl alcohol (BnOH, puriss., 99–100.5% (GC)), 2-amino-2-(hydroxymethyl)-1,3-propanediol (Trizma base, puriss., ≥ 99.7%), palladium(II) acetate ($Pd(ac)_2$, ≥ 99.9% trace metals basis), and methanol (MeOH, analytical grade) were purchased from Sigma-Aldrich. Acetone (99.8%, extra dry) and chloroform (≥ 99%, extra pure) were purchased from Acros Organics. Ethanol (absolute, > 99.8% for analysis) and diethyl ether (≥99.5%) were purchased from VWR Chemicals. Liquid carbon dioxide (≥99%), argon (Ar, 99.999%), helium (He, 99999%), nitrogen (N_2, 99.999%), and various calibration gases were provided by PanGas AG, Switzerland. All chemicals were used as received without further purification.

Synthesis of the TiO_2 Nanoparticle Dispersion: Trizma-functionalized TiO_2 nanoparticles were synthesized according to a modified route by Niederberger and co-workers.[50] 414 mg (3.4 mmol) of Trizma were dissolved in 90 mL of BnOH in an oil bath set at 80 °C under ambient atmosphere. After cooling the solution to room temperature, 4.5 mL (40.9 mmol) of $TiCl_4$ were added under vigorous stirring. Subsequently, the reaction solution was heated again to 80 °C and kept at this temperature for 24 h. The white precipitate was separated from the solution by centrifugation and washed three times with chloroform and three times with diethyl ether in that order. The still wet, white powder was dispersed in 30 mL of deionized water. Residual diethyl ether was removed by application of a vacuum.

Synthesis of the Pd Nanoparticle Dispersion: The Pd nanoparticles were synthesized according to the route reported by Staniuk et al.[51] $Pd(ac)_2$ (32 mg, 0.14 mmol) was dispersed in 4 mL of anhydrous BnOH inside a glove box under Ar atmosphere. The sealed glass vessel was transferred onto a stirring plate outside the glove box and the mixture was stirred for 18 h at room temperature. The black precipitate was collected from the solution by centrifugation and washed three times with ethanol. After the last centrifugation step, the supernatant was decanted and the still wet products of four syntheses were mixed with 40 mL of ethanol. Subsequently, the concentration in mg mL^{-1} of the dispersion was determined by taking the average of the dry weight of three times 1 mL of the dispersion. Additional ethanol was added to the dispersion to arrive at 0.34 wt% Pd in ethanol.

Printing of the Polymeric Scaffolds: The plane scaffold structure based on a diamond lattice was downloaded from the online platform thingiverse (www.thingiverse.com) and further modified in Autodesk Meshmixer (Autodesk, www.meshmixer.com). All lattices have a strut thickness of 200 μm and a unit cell size of 2.5 × 2.5 × 2.5 mm. This geometry was extended to a cylindrical size of 10.4 mm diameter and 20 mm length to obtain the standard scaffold geometry (Figure 1a,e). Furthermore, scaffolds with a length of 10, 15, and 30 mm were realized.

To assess the penetration depth of the UV light, scaffolds with solid cores were produced (Figure 1b,f). The cores had a diameter of 1, 3, 5 or 7 mm (Figure 1c). Additionally, scaffolds with cores with an elliptic base (semiminor axis = 5 mm, semimajor axis = 10.4 mm) were printed. Finally, a scaffold with a cylindrical, hollow core of 3.75 mm outer and 3 mm inner diameter was designed. The cylinder contained holes with 0.5 mm diameter, which were arranged in layers of 1.5 mm distance and at a 45° angle to each other. To allow for tight sealing in the continuous gas flow reactor and a controlled gas flow, the cylinder was closed on one side and had a cylindrical opening with a rim width of 2 mm on the other side (Figure 1d).

All 3D scaffold models were virtually sliced in layers using Print Studio (Autodesk, Version 1.6.5) and printed with a commercially available acrylate-based resin (Ember PR48, Autodesk) on a desktop digital light processing printer (Ember 3D Printer, Autodesk). The layer height was set to 25 μm, which were illuminated for 3 s at 20 mW cm^{-2} for best resolution.

TiO_2–Pd Aerogel Fabrication: The colloidal TiO_2 and Pd nanoparticle dispersions were combined in a ratio of 1:1 (v/v) under continuous stirring. This mixture was transferred into quartz tubes (inner diameter 10.4 mm, outer diameter 13 mm, length 1 cm, 2 cm, or 3 cm) containing the 3D printed polymeric scaffolds (Figure 1). Quartz tubes and scaffolds had been placed into cut open 10 mL syringe setups (Figure S8, Supporting Information) before. This setup facilitates the removal of the gels after the gelation inducing heat-treatment at 60 °C for 30 min in a saturated ethanol atmosphere. The formed gray-blue translucent gels completely surrounded the scaffolds in the quartz tubes. After taking the samples out of the gelation oven, the quartz tubes including scaffolds and gels were immediately immersed into an ethanol–water 1:1 (v/v) mixture to avoid drying and cracking. Over the course of some days, the pore liquid in the gel was gradually exchanged to 100% acetone in 10% steps, each lasting 8–12 h. As a final step, the gels were supercritically dried in an SPI-DRY Critical Point Dryer 13200 exchanging the acetone with liquid CO_2. The aerogels including the scaffolds inside the quartz tubes were treated with high intensity UV light (2000 W) for 20 h under ambient atmosphere to remove surface organics using a Honle UVACUBE2000 (Mercury UV lamp, arc power output 100 W cm^{-1}).

Characterization: Powder XRD measurements of ground TiO_2–Pd aerogels and of the Pd nanoparticles were conducted on an Empyrean (PANalytical B.V., The Netherlands) diffractometer equipped with a PIXcel 1D detector and operating in reflection mode with Cu Kα radiation. Taking advantage of the effect of peak broadening, the mean crystallite sizes of the TiO_2 and Pd nanoparticles were calculated from the full width at half maximum of the (101) and the (111) reflections, respectively, using the Scherrer equation. SEM studies of the TiO_2–Pd aerogel and of the Pd nanoparticles were performed on a FEI Magellan 400 and on a Zeiss Leo-1530 microscope, respectively. Prior to SEM analysis, the aerogel samples and the Pd nanoparticles were coated with 3 nm Pt and with 6 nm Pt, respectively. TGA was performed on UV and non-UV pretreated TiO_2–Pd aerogel samples using a TGA/DSC 3_+ $STAR_e$ SYSTEM by Mettler Toledo. The samples were first heated to 110 °C for 20 min under air atmosphere to remove any water adsorbed to the surface. Subsequently, the samples were ramped (10 °C min^{-1}) to 900 °C. Gas sorption experiments were performed on a Quantachrome Autosorb iQ using N_2 at 77 K. Before the measurement, the samples were outgassed at 100 °C for at least 24 h. The surface area was determined via the Brunauer–Emmett–Teller method and the pore size and pore volume by density functional theory (DFT) analysis using a non-local DFT (NLDFT) sorption model for N_2 at 77 K based on cylindrical silica pores. X-ray photoelectron spectra were recorded on a Sigma 2 spectrometer (Thermo Scientific) using a polychromatic Mg Kα X-ray source with C1s = 284.8 eV.

Photocatalytic Measurements: The photocatalytic hydrogen evolution of the various aerogel monoliths was analyzed using a customized continuous gas flow reactor (Scheme 1). Ar gas was bubbled through a bath at room temperature to enrich it with water and MeOH (1:1 v/v) at a flow rate of 5 mL min^{-1}, which was controlled by a mass flow meter (Cole–Parmer) and a needle valve (VICI Valco Instruments Co. Inc.). The gas was directed to the reaction cell, consisting of a quartz tube (Robson Scientific, 14 mm inner diameter), which was connected to the rest of the tubing with custom-build ISO-KF connectors to ensure gas tightness.[38] The aerogel monoliths plus scaffolds inside the short quartz tubes were fixed inside the quartz tube of the reaction cell with a combination of Teflon rings and NBR O-rings to ensure the interaction of the gas with the aerogel. On opposite sides and at a 90° angle to the reaction cell, two Thorlabs mounted high-power LEDs with a wavelength of 375 nm (M375L4) were installed at a distance of 1 cm from the quartz tube. The outlet of the reaction cell was connected to a gas chromatograph (Inficon Micro-GC 3000A, equipped with He and Ar carrier gas and four separate modules, each consisting of an individual injector system, column and µ-TCD detector, twice 10 m Molsieve × 30 µm, 8 m PLOT Q/1m PLOT Q × 10 µm with backflush injector and 20 m OV-1 × 2 µm, various calibration gases were used to calibrate the GC). Gas samples were collected every 5 min. A typical measurement started with a purging phase, during which the reaction cell including the aerogel and all the tubing was flushed with humidified gas under no illumination, to eliminate oxygen. This phase was followed by the analysis of the hydrogen production of the aerogel under light illumination for a minimum of 2 and up to 24 h.

By default, the hydrogen production rate was calculated in µmol of produced hydrogen per measured mass of photocatalyst in gram and hour of illumination time (i.e., µmol g^{-1} h^{-1}) using the absolute amount of hydrogen produced after 10 h of illumination. After 10 h, it was certain that the production reached a linear behavior and different samples could be compared directly. However, if the samples to be compared showed a very similar hydrogen production behavior over time from the start, the hydrogen production rate was calculated using the absolute amount of hydrogen produced after only 2 h of illumination. This was done to save time and, simultaneously, to obtain an average hydrogen production rate with a standard deviation from three identical samples.

Supporting Information

Supporting Information is available from the Wiley Online Library or from the author.

Acknowledgements

The authors gratefully acknowledge the financial support by the Swiss National Science Foundation (Project 200020B_184842) and by ETH Zürich. The authors thank Till Kyburz for technical assistance and Livia Schneider, Manuel Bertsch, and Yannick Kürsteiner for experimental assistance. Prof. Nicholas Spencer and Prof. Antonella Rossi are acknowledged for access to their X-ray photoelectron spectrometer. The authors also thank the Scientific Center for Optical and Electron Microscopy (ScopeM) of ETH Zürich for providing access to the electron microscopy facilities.

Open access funding provided by Eidgenossische Technische Hochschule Zurich.

Conflict of Interest

The authors declare no conflict of interest.

Data Availability Statement

Research data are not shared.

Keywords

3D printing, aerogels, hydrogen production, nanoparticles, photocatalysis, TiO_2

Received: July 13, 2021
Revised: August 30, 2021
Published online: October 17, 2021

[1] J. A. Turner, *Science* **2004**, *305*, 972.
[2] S. E. Hosseini, M. A. Wahid, *Renewable Sustainable Energy Rev.* **2016**, *57*, 850.
[3] M. Schreck, M. Niederberger, *Chem. Mater.* **2019**, *31*, 597.
[4] C. Xu, P. R. Anusuyadevi, C. Aymonier, R. Luque, S. Marre, *Chem. Soc. Rev.* **2019**, *48*, 3868.
[5] A. Kudo, Y. Miseki, *Chem. Soc. Rev.* **2009**, *38*, 253.
[6] J. Schneider, M. Matsuoka, M. Takeuchi, J. Zhang, Y. Horiuchi, M. Anpo, D. W. Bahnemann, *Chem. Rev.* **2014**, *114*, 9919.
[7] X. Zhou, N. Liu, J. Schmidt, A. Kahnt, A. Osvet, S. Romeis, E. M. Zolnhofer, V. R. R. Marthala, D. M. Guldi, W. Peukert, M. Hartmann, K. Meyer, P. Schmuki, *Adv. Mater.* **2017**, *29*, 1604747.
[8] M. Bernareggi, G. L. Chiarello, G. West, M. Ratova, A. M. Ferretti, P. Kelly, E. Selli, *Catal. Today* **2019**, *326*, 15.
[9] D. W. Su, J. Ran, Z. W. Zhuang, C. Chen, S. Z. Qiao, Y. D. Li, G. X. Wang, *Sci. Adv.* **2020**, *6*, 8447.
[10] Y. H. Yu, Y. P. Chen, Z. Cheng, *Int. J. Hydrogen Energy* **2015**, *40*, 15994.
[11] M. Berr, A. Vaneski, A. S. Susha, J. Rodríguez-Fernández, M. Döblinger, F. Jäckel, A. L. Rogach, J. Feldmann, *Appl. Phys. Lett.* **2010**, *97*, 093108.
[12] J. Liang, Y. Chai, L. Li, *Cryst. Res. Technol.* **2017**, *52*, 1700022.
[13] M. Ge, Q. Li, C. Cao, J. Huang, S. Li, S. Zhang, Z. Chen, K. Zhang, S. S. Al-Deyab, Y. Lai, *Adv. Sci.* **2017**, *4*, 1600152.
[14] J. Yoo, M. Altomare, M. Mokhtar, A. Alshehri, S. A. Al-Thabaiti, A. Mazare, P. Schmuki, *J. Phys. Chem. C* **2016**, *120*, 15884.
[15] N. T. Nguyen, S. Ozkan, S. Hejazi, N. Denisov, O. Tomanec, R. Zboril, P. Schmuki, *Int. J. Hydrogen Energy* **2019**, *44*, 22962.
[16] Y. Okamoto, S. Ida, J. Hyodo, H. Hagiwara, T. Ishihara, *J. Am. Chem. Soc.* **2011**, *133*, 18034.

[17] B. Mahler, V. Hoepfner, K. Liao, G. A. Ozin, *J. Am. Chem. Soc.* **2014**, *136*, 14121.
[18] L. Shang, B. Tong, H. Yu, G. I. N. Waterhouse, C. Zhou, Y. Zhao, M. Tahir, L. Z. Wu, C. H. Tung, T. Zhang, *Adv. Energy Mater.* **2016**, *6*, 1501974.
[19] W. Wan, R. Zhang, M. Ma, Y. Zhou, *J. Mater. Chem. A* **2018**, *6*, 754.
[20] N. Alenzi, W. S. Liao, P. S. Cremer, V. Sanchez-Torres, T. K. Wood, C. Ehlig-Economides, Z. Cheng, *Int. J. Hydrogen Energy* **2010**, *35*, 11768.
[21] R. Shwetharani, H. R. Chandan, M. Sakar, G. R. Balakrishna, K. R. Reddy, A. V. Raghu, *Int. J. Hydrogen Energy* **2020**, *45*, 18289.
[22] C. J. Chang, P. Y. Chao, *Int. J. Hydrogen Energy* **2019**, *44*, 20805.
[23] Y. Su, S. Li, D. He, D. Yu, F. Liu, N. Shao, Z. Zhang, *ACS Sustainable Chem. Eng.* **2018**, *6*, 11989.
[24] C. Jiang, K. Y. Lee, C. M. A. Parlett, M. K. Bayazit, C. C. Lau, Q. Ruan, S. J. A. Moniz, A. F. Lee, J. Tang, *Appl. Catal. A* **2016**, *521*, 133.
[25] D. Pan, Z. Han, Y. Miao, D. Zhang, G. Li, *Appl. Catal., B* **2018**, *229*, 130.
[26] Q. Wang, Y. Chen, R. Liu, H. Liu, Z. Li, *Composites, Part A* **2012**, *43*, 1869.
[27] J. Zhang, F. Huang, *Appl. Surf. Sci.* **2015**, *358*, 287.
[28] J. Fu, B. Zhu, W. You, M. Jaroniec, J. Yu, *Appl. Catal., B* **2018**, *220*, 148.
[29] T. Yan, N. Li, Z. Jiang, W. Guan, Z. Qiao, B. Huang, *Int. J. Hydrogen Energy* **2018**, *43*, 20616.
[30] X. Chen, R. Shi, Q. Chen, Z. Zhang, W. Jiang, Y. Zhu, T. Zhang, *Nano Energy* **2019**, *59*, 644.
[31] M. Krishnappa, V. S. Souza, N. Ganganagappa, J. D. Scholten, S. R. Teixeira, J. Dupont, R. Thippeswamy, *Chem. - Eur. J.* **2015**, *21*, 17624.
[32] W. Zhang, Y. Li, S. Peng, *ACS Appl. Mater. Interfaces* **2016**, *8*, 15187.
[33] Q. Liang, Z. Li, X. Yu, Z. H. Huang, F. Kang, Q. H. Yang, *Adv. Mater.* **2015**, *27*, 4634.
[34] R. Zhang, W. Wan, D. Li, F. Dong, Y. Zhou, *Chin. J. Catal.* **2017**, *38*, 313.
[35] H. Ou, P. Yang, L. Lin, M. Anpo, X. Wang, *Angew. Chem.* **2017**, *129*, 11045.
[36] P. A. DeSario, J. J. Pietron, A. Dunkelberger, T. H. Brintlinger, O. Baturina, R. M. Stroud, J. C. Owrutsky, D. R. Rolison, *Langmuir* **2017**, *33*, 9444.
[37] G. A. Ozin, *Energy Environ. Sci.* **2015**, *8*, 1682.
[38] F. Rechberger, M. Niederberger, *Mater. Horiz.* **2017**, *20*, 2831.
[39] M. Odziomek, F. Chaput, F. Lerouge, C. Dujardin, M. Sitarz, S. Karpati, S. Parola, *Chem. Mater.* **2018**, *30*, 5460.
[40] D. Wen, A. Eychmüller, *Chem. Commun.* **2017**, *53*, 12608.
[41] P. Rusch, D. Zámbó, N. C. Bigall, *Acc. Chem. Res.* **2020**, *53*, 2414.
[42] A. L. Luna, F. Matter, M. Schreck, J. Wohlwend, E. Tervoort, C. Colbeau-Justin, M. Niederberger, *Appl. Catal., B* **2020**, *267*, 118660.
[43] F. Matter, A. L. Luna, M. Niederberger, *Nano Today* **2020**, *30*, 100827.
[44] J. Fricke, A. Emmerling, *J. Am. Ceram. Soc.* **1992**, *75*, 2027.
[45] P. Gomathisankar, D. Yamamoto, H. Katsumata, T. Suzuki, S. Kaneco, *Int. J. Hydrogen Energy* **2013**, *38*, 5517.
[46] M. Bowker, C. Morton, J. Kennedy, H. Bahruji, J. Greves, W. Jones, P. R. Davies, C. Brookes, P. P. Wells, N. Dimitratos, *J. Catal.* **2014**, *310*, 10.
[47] N. Abdullah, H. Bahruji, S. M. Rogers, P. P. Wells, C. R. A. Catlow, M. Bowker, *Phys. Chem. Chem. Phys.* **2019**, *21*, 16154.
[48] B. Hosticka, P. M. Norris, J. S. Brenizer, C. E. Daitch, *J. Non-Cryst. Solids* **1998**, *225*, 293.
[49] THORLABS, SpecSheet Mounted LED, 375 nm, https://www.thorlabs.com/drawings/6fe6f0a957d8d375-0984D2BE-9638-C67D-5351C1D8A97FE861/M375L4-SpecSheet.pdf (accessed: April 2021).
[50] J. Polleux, N. Pinna, M. Antonietti, C. Hess, U. Wild, R. Schlögl, M. Niederberger, *Chem. - Eur. J.* **2005**, *11*, 3541.
[51] M. Staniuk, F. Rechberger, E. Tervoort, M. Niederberger, *J. Sol-Gel Sci. Technol.* **2020**, *95*, 573.